Distortions of inertia waves in a rotating fluid cylinder forced near its fundamental mode resonance

By RICHARD MANASSEH†

Department of Applied Mathematics and Theoretical Physics, University of Cambridge,
Silver Street, Cambridge CB3 9EW, UK

A series of experimental observations is presented of a flow in which inertial oscillations are excited. The homogeneous fluid is contained in a completely filled right circular cylinder. The cylinder is spun about its axis of symmetry and a small 'forced precession' (or coning motion) is impulsively started. The flow is visualized by an electrolytic dyeline method. The mathematical problem for linear inviscid inertial oscillations in this system, although ill-posed in general, admits a solution in terms of wave modes for the specific boundary conditions considered here. The experiments show that while this linear inviscid theory provides some facility for predicting the flow structure at early times, the flow rapidly and irreversibly distorts away from the predicted form. This behaviour is seen as a precursor to some of the more dramatic breakdowns described by previous authors, and it may be pertinent to an understanding of the breakdowns reported in experiments on elliptical flow instabilities.

1. Introduction

In general, the system under consideration is homogeneous fluid completely filling a spinning container, and subjected to some form of external forcing. The specific fluid system studied in this paper is contained in a right circular cylinder spinning steadily about its axis of symmetry. The fluid was supposed to have attained solid-body rotation before the commencement of forcing, in which there is initially no fluid motion relative to the container walls. The forcing was due to a small 'precession' of the axis of spin: this axis itself rotated in inertial space to trace out the surface of a double cone. The apexes of these cones are together at the container centroid.

For inertial oscillations in a cylindrical container, the dispersion relation giving the eigenfrequencies of linear inviscid normal modes was first derived by Kelvin (1880) and its predictions for the eigenfrequencies were tested experimentally by Fultz (1959), McEwan (1970), Stergiopoulos & Aldridge (1982) and Manasseh (1992).

McEwan (1970) measured the amplitude of the oscillations using a thermistor probe. He found reasonable agreement of the amplitude–cylinder-height spectrum with the linear inviscid theory, near the lowest-order mode he could force. To do this he had to include modes with radial wavenumbers up to 5 in the theoretical spectrum.

† Current affiliation: School of Mathematics, University of New South Wales, P.O. Box 1, Kensington, NSW 2033, Australia

However, he found the resolution of the spectrum to be 'poor', responding essentially to the lowest-order mode that could be forced.

Several experimental studies of rotating fluid systems in which inertial modes arise (for example Malkus 1968; McEwan 1970; and Manasseh 1992) have documented fluid flow breakdowns leading to turbulence. Manasseh (1992) described a system kinematically identical to the one in this paper, but made a wider and less detailed survey of the parameter space. Different breakdown regimes were catalogued by a letter scheme (A–G), where a Type A breakdown results in the generation of turbulence with the smallest scales. Manasseh (1992) described flow visualizations by means of a reflective flake technique that provided an excellent picture of the flow structure, but gave no information on fluid velocities. Quantitative data were extracted in the form of the times for the breakdowns to occur. The breakdown phenomena, while readily produced over a large region of parameter space, appeared to be complex and varied.

The cause or causes of the breakdowns remain unclear. There is some experimental evidence of nonlinear interactions between inertial modes in a cylinder (Aldridge & Stergiopoulos 1991; Manasseh 1992). In Aldridge & Stergiopoulos (1991) a least-squares procedure was used to recover the time-dependent eigenfrequencies corresponding to freely decaying modes in a cylindrical cavity. The decay rates of some modes were found to vary with time. An interpretation of this has the mode amplitudes slowly oscillating with time, due to nonlinear interactions. In Manasseh (1992) visual observations, quantified by image-processing measurements, were made of higher-order modes than those directly forced. Normally, such evidence would prompt the use of a weakly nonlinear or low-order dynamical systems model, based on a low number of modes. However, the inertial modes in a cylinder cannot be conveniently grouped into resonant triads, owing to the nature of their dispersion relation, preventing a simple implementation of weakly nonlinear theory. Furthermore, it is only in a small region of parameter space that a low number of modes appears to be interacting.

Some breakdown phenomena are associated with a mean flow taking the form of an azimuthal circulation relative to the container walls. The participation of an azimuthal circulation in resonant collapse was suggested by both McEwan (1970) and Gunn & Aldridge (1990). Although linear inviscid theory predicts only oscillatory flow under oscillatory forcing, wave-mean flow interactions (see, for example, McIntyre & Norton 1990) occur when some dissipation and nonlinearity are permitted. An asymptotic analysis by Thompson (1970) predicted a small mean flow $O(\theta)$ times the first-order forced response amplitude, where θ is the small parameter used in the analysis.

Recent interest in elliptical flow instabilities (Gledzer, Dolzhanskii & Obukhov 1989; Malkus 1989; Waleffe 1990; Malkus & Waleffe 1991; Gledzer & Ponomarev 1992; Kerswell 1993) has broadened the relevance of the inertia wave breakdown phenomena. An inertia wave mode can be shown (Waleffe 1990) to be the fastest growing unstable mode in the instability of an elliptical flow. It was suggested by Malkus & Waleffe (1991) that the subsequent breakdown of the inertial mode is a 'ubiquitous source of turbulence which by-passes lesser chaotic phases'.

A practical application lies in the control of spinning spacecraft carrying liquid fuels, for which inertial oscillations and their prevention are of current research interest (Scott & Tan 1993; Manasseh 1993).

The first and main objective of the experiments reported here was to gain further insight into the flows reported in McEwan (1970) and Manasseh (1992), by using a

different flow visualization technique that provides some information on the magnitude of velocity in the flow. A specific aim was to determine if the dyeline pattern before breakdown corresponded to that predicted by linear inviscid theory. The experiments were to be conducted near the resonances of low-order modes, so that relatively simple structures should develop for easy comparison with theory. The single low-order mode closest to resonance was expected to dominate the flow – although other, high-order, modes would have resonances nearby owing to the unusual nature of the dispersion relation, these would be damped by viscosity. This paper is restricted to describing the experiments near the lowest-order mode that could be forced: the 'fundamental' mode. A second objective, which was only partly met, was to determine if an azimuthal circulation was a significant participant in the breakdown of the flow.

The linear inviscid theory is presented in §2 in outline form only, since it has already been detailed in Manasseh (1992). The experimental techniques are described §3 and a guide to interpreting the experimental results is in §4. A description of a calculation used to compare the predictions of linear inviscid theory with the early stages of the experiments is in §5, while the actual experimental results are in §6.

2. Linear inviscid theory

Referring to figure 1, which defines some basic parameters, consider a general fluid-filled container spinning about an axis through its centroid and precessing about a second axis through its centroid. Assume the centroid is not accelerating in inertial space, and the angle between the two axes is not varying with time. In rotating fluid dynamics problems one typically chooses the basic rotation period of the fluid relative to inertial space as the timescale; in our problem this is $\Omega^{-1} = |(\omega_1 \hat{k} + \omega_2 \hat{K})|^{-1}$. Here, however, we will choose the timescale to be ω_1^{-1}. In making this choice of timescale, we are anticipating observing experiments from a frame of reference in which periods of $2\pi/\omega_1$ are easily counted to provide a timescale with which various events can be measured. In fact, in the experiments to be described later, $2\pi/\omega_1$ is the rotation period of the tank relative to the observing cameras. The lengthscale D is equal to the container diameter. The cylinder length/diameter aspect ratio is h. We assume that the *nutation angle* θ between the two axes is small, and assuming that the velocity scale $U = O(\omega_1 D\theta)$ allows linearization of the problem. The dimensional pressure is $\rho\omega_1 UDp$, where p is the dynamic pressure in excess of the centrifugal pressure that plays no dynamical role in this problem. The non-dimensional excitation frequency ω is defined as twice the ratio of the basic rotation rate Ω to first order in θ, to the frequency of the variation of the overall angular velocity vector in tank coordinates, ω_1, giving

$$\omega = 2(1 + \frac{\omega_2}{\omega_1}). \qquad (2.1)$$

The incompressible inviscid linearized fluid equation of motion relative to axes *fixed in the container* is

$$\frac{\partial u}{\partial t} + \omega\hat{k} \times u + \nabla p = -(\omega - 2)(r\cos(\phi + t))\hat{k}, \qquad (2.2)$$

together with continuity,

$$\nabla \cdot u = 0 . \qquad (2.3)$$

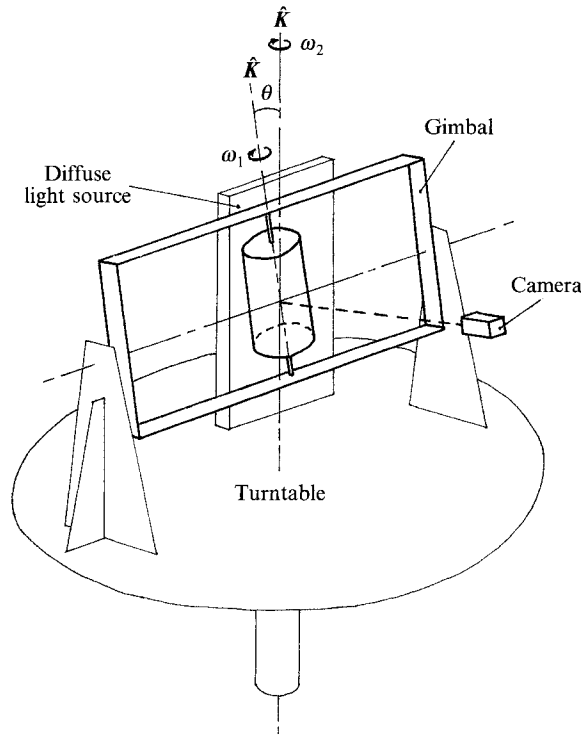Equation (2.2) is the form of the momentum equation appropriate to our problem;

R. Manasseh

FIGURE 1. Schematic drawing of the apparatus.

steps in its derivation are outlined in Wood (1966). The boundary condition is

$$\boldsymbol{u} \cdot \hat{\boldsymbol{n}} = 0 \,, \tag{2.4}$$

where $\hat{\boldsymbol{n}}$ is the unit normal vector to the container surface. This allows a free-slip condition at the container wall consistent with the assumption of an inviscid flow. To effect the inviscid approximation, an Ekman number, defined by $E = \nu/(\omega_1 D^2)$, has been assumed to be negligibly small. The dimensional *spin-up time* is given by

$$t_s = \frac{D}{(\omega_1 + \omega_2)^{\frac{1}{2}} \nu^{\frac{1}{2}}} \,. \tag{2.5}$$

Adopt cylindrical polar coordinates (r, ϕ, z) fixed in the tank, with their origin at the cylinder centroid. Assuming a separable solution to the homogeneous version of (2.2), of form

$$\boldsymbol{u} = \sum_{n=1}^{\infty} \boldsymbol{U}_n \, \mathrm{e}^{\mathrm{i}t}, \tag{2.6}$$

$$p = \sum_{n=1}^{\infty} Q_n(r, \phi, z) \, \mathrm{e}^{\mathrm{i}t}, \tag{2.7}$$

and eliminating the velocity components with the aid of the continuity equation, we get Poincaré's equation,

$$\frac{1}{r} \frac{\partial}{\partial r} \left(r \frac{\partial Q_n}{\partial r} \right) + \frac{1}{r^2} \frac{\partial^2 Q_n}{\partial \phi^2} + (1 - \omega^2) \frac{\partial^2 Q_n}{\partial z^2} = 0 \,, \tag{2.8}$$

k	l	ω_{kl1}	λ_{kl1}	k	l	ω_{kl1}	λ_{kl1}
1	1	2.64298	2.88221	4	1	1.12769	2.45622
1	2	5.27757	6.10489	4	2	1.55603	5.61787
1	3	7.93621	9.27678	4	3	2.11440	8.77909
2	1	1.48403	2.58361	5	1	1.08229	2.43833
2	2	2.65374	5.79180	5	2	1.37830	5.58728
2	3	3.93395	8.96470	5	3	1.78975	8.74335
3	1	1.22370	2.49274	6	1	1.05736	2.42833
3	2	1.89134	5.67380	6	2	1.27306	5.56886
3	3	2.69398	8.84105	6	3	1.58812	8.72081

TABLE 1. Resonant excitation frequencies ω_{klm} and radial wavenumbers λ_{klm} for a precessionally forced cylinder, $h = 4/3$

a hyperbolic p.d.e. for $|\omega| > 1$. The associated boundary condition is

$$U \cdot \hat{n} = 0. \tag{2.9}$$

In an unbounded domain (2.8) admits a set of plane-wave solutions, which are usually referred to in the literature as *inertia waves*. Although the full problem given by (2.8) and (2.9) is ill-posed, it is possible to find an analytic description of the flow in the case of the particular geometry of a right circular cylinder.

For brevity, the index n is used to indicate a unique combination of the spatial wavenumbers k, λ and m. The integer k is the axial wavenumber and the integer m is the azimuthal wavenumber. As the radial wavenumber λ is non-integer, it is convenient to use an integer index l to count the number of half-cycles in the radial direction.

A solution to (2.8) and (2.9) by separation of variables is

$$Q_n = J_m(2\lambda_n r) \cos(2(\omega^2 - 1)^{-\frac{1}{2}} \lambda_n [z + h/2]) \, e^{im\phi} \,, \tag{2.10}$$

where J_m is the Bessel function of the first kind, order m. A solution to Poincaré's equation of this kind was first found by Kelvin (1880).

Resonant excitation frequencies ω_n correspond to eigenvalues of the system for this particular geometry and for precessional forcing, which requires modes with $m = 1$. Some of the lower-order ω_n are tabulated in table 1 for the cylinder length / diameter ratio h of this experiment.

Note that the ω_n do not increase monotonically with increasing order of the wavenumber vector. The ω_n are densely spaced; for any ω_n, it is possible to find another arbitrarily close.

The velocity field $u = \text{Re} \sum_{n=1}^{\infty} (A_n U_n \, e^{it})$ that solves (2.2), is given by

$$u = \sum_{n=1}^{\infty} A_n \left\{ -\frac{1}{1 - \omega_n^2} \left[\frac{dJ_1(2\lambda_n r)}{dr} + \omega_n \frac{1}{r} J_1(2\lambda_n r) \right] \cos \left[k\pi(z/h + \tfrac{1}{2}) \right] \sin(\phi + t) \right.$$

$$\frac{-1}{1 - \omega_n^2} \left[\omega_n \frac{dJ_1(2\lambda_n r)}{dr} + \frac{1}{r} J_1(2\lambda_n r) \right] \cos \left[k\pi(z/h + \tfrac{1}{2}) \right] \cos(\phi + t)$$

$$\left. \frac{k\pi}{h} J_1(2\lambda_n r) \sin \left[k\pi(z/h + \tfrac{1}{2}) \right] \sin(\phi + t) \right\} \tag{2.11}$$

and the pressure by

$$p = \sum_{n=1}^{\infty} \frac{\omega}{\omega_n} A_n J_1(2\lambda_n r) \cos\left[k\pi(z/h + \tfrac{1}{2})\right] \cos(\phi + t). \qquad (2.12)$$

The amplitudes A_n are found by calculating the inner-product integral of the forcing function which is on the right-hand side of (2.2), using the spatial structure of the nth mode. The calculation of the A_n is presented in the Appendix to this paper.

In principle we could force all the linear inviscid modes, up to the order where the wavelength is comparable to the boundary-layer thickness. However, the modes that can be precessionally forced have $m = 1$, as noted above. Furthermore, the forcing function, $-(\omega - 2)(r\cos(\phi + t))\hat{k}$, is even in z, so the modes upon which it will project must have a vertical velocity that is also even in z, requiring, from (2.11), an odd axial wavenumber k. As in Manasseh (1992), low-order modes are those with a small wavenumber vector magnitude.

3. Experimental apparatus, technique and procedure

3.1. *Apparatus and technique*

Full details of the apparatus and technique are in Manasseh (1991). Figure 1 is a schematic diagram of the apparatus which realized the precessing tank system. The Perspex tank is of internal diameter 90 mm and internal height 120 mm. It spins in a gimbal frame which is in turn mounted on a turntable. Here ω_1 is the spin rate of the tank relative to the gimbal frame and the precession rate ω_2 is the spin rate of the turntable relative to the laboratory. The nutation angle θ can be varied by tilting the gimbal frame from the vertical. For the experiments reported in this paper, the tank spin axis was precessed at a constant θ which was small (1°). To do this, the system was first spun up to a desired combination of ω_1 and ω_2, with $\theta = 0$. Precession, and hence forcing, was initiated by an impulsive tilt of the gimbal frame to the preset value of 1°. The fluid was illuminated by a diffuse fluorescent light source and viewed by a video camera or a still camera fixed on the turntable.

The experiments were performed at the Department of Applied Mathematics and Theoretical Physics (DAMTP) at Cambridge University. A DAMTP precision turntable was used; it is driven by a permanent magnet D.C. servomotor controlled by an analog loop, feedback being provided by an integral tachogenerator. The reference voltage is supplied by a BBC microcomputer with 16 bits resolution, which also controlled the experimental procedure for the experiments reported here.

The thymol blue electrolytic dyeline technique (Baker 1966) utilizes the colour change of thymol blue indicator molecules in the presence of a local concentration of base ions. Thymol blue crystals are first dissolved in the fluid, which is distilled water. The fluid is then made into an appropriate electrolyte by the addition of acid and base solutions. This ambient fluid is orange-yellow in colour. If a low (5 to 10 V) potential is applied to the fluid by electrodes, H^+ ions will collect at the cathode, forming a local deficit of OH^- ions which react with the indicator molecules to form a dark blue dyed zone. If the applied voltage is switched off, the indicator will eventually revert to its original colour; the technique can thus be used continuously in a small fluid volume. In the meantime, fluid motion carries the dyed patch away from the cathode, permitting a visualization of the flow.

A stainless steel wire of diameter 0.05 mm was used as the cathode. In the experiments reported in this paper, a single wire was used. It was mounted slant-wise

in the tank with the ends of the wire mounted on the flat endwalls of the cylinder at a radius of 12.5 mm. The anode was a single brass screw at one end of the tank at a radius of 12.5 mm. A slanting orientation was chosen so that both axial and horizontal velocities would cause a noticeable departure of dye from the wire. Trial estimations of fluid velocity, made as described in §6, gave fluid flows of order 10 mm s^{-1} relative to the wire, corresponding to a Reynolds number for the wire of about 0.5. Laminar vortex shedding from a cylinder does not begin until the Reynolds number reaches about 50. Thus, in respect of spurious oscillatory disturbances, the wire has a negligible influence on the flow. In the visualizations there was no evidence of vortices being shed from the wire. The possibility of other influences from the wire is discussed at the end of §6 and in §7.

The experiments of McEwan (1970) and Manasseh (1992), which both used a reflective flake technique, reported difficulties in achieving solid-body rotation. In Manasseh (1992) a 'bright column' along the cylinder axis was noted, implying a relative shear in the fluid after several spin-up times had elapsed. The reflective flakes are aligned by any strain field above the level of that due to Brownian motion, irrespective of the magnitude of the velocities involved, and so the magnitude of the flow corresponding to the 'bright column' was uncertain. Initial tests using the thymol blue technique indicated that the bright column present before the commencement of forcing did in fact correspond to a small anticyclonic departure from solid-body rotation. This departure was called the 'anomaly drift' (Manasseh 1991). Careful calibrations were performed. (These included a study of the very slow 'intrinsic' drift of the dyeline in a motionless tank that was probably due to the asymmetry in the electric field.) Optimal settings were found that minimized the anomaly drift and rendered the intrinsic drift negligible. In Manasseh (1991) the anomaly drift was shown to be at most 1/100 of the forced flow velocity and it was ascribed to small irregularities in the container spin rate. It was inferred that the behaviour in a system free of anomaly drifts was unlikely to be different, given a forced flow velocity typically 100 times larger.

3.2. *Experimental procedure*

The procedure during the experiments reported in §6 was as follows:

The tank was set spinning for about 2 hours. Tests had shown that the anomaly drift reduced to a stable value after about 2 hours. The tank spin rate ω_1 was stroboscopically checked and set using an analog controller. The tank was left spinning throughout the set of experimental runs.

The procedure during each run was as follows:

1. The tank spin and turntable axes were set to be collinear. The turntable was spun up to a speed calculated by the microcomputer.

2. The theoretical spin-up time given by (2.5) was allowed to pass.

3. An additional period elapsed to ensure that any flows from a previous run had dissipated. The total wait time was at least 100 revolutions of the tank in inertial space, about 4 spin-up times for experiments conducted near the (1,1,1) mode resonant frequency.

4. The video recorder began recording. The dyeline current was switched on for 60 s, which was the optimum time determined by tests detailed in Manasseh (1991).

5. The gimbal locking catch was released to initiate forcing.

6. The turntable was spun down and the axes returned to collinear.

There were 4 runs at the same parameter settings to ensure repeatability of the results.

4. Predictions of linear inviscid theory

We can deduce how the dyeline should appear from the turntable frame of reference from which the video recordings were made and the photographs taken. The approximations of linearity and inviscid flow still hold. The dye particles, under the influence of forced inertia wave modes, should follow orbital paths relative to tank-fixed coordinates, just as particles in the ocean trace out orbital paths under the influence of surface gravity waves. The dye particles should rotate on their orbits with the forcing frequency $-\omega_1$ relative to tank-fixed coordinates, while the tank and wire fixed in it are rotating relative to the camera with the opposite frequency, ω_1. Figure 2 is an idealized diagram of this motion, near the tank ends where the motion is essentially normal to the axis. The 'radius' of the orbits (idealized as circular) will increase as the amplitude of the oscillation increases. As with any forced linear oscillator, the amplitude depends linearly on the forcing amplitude and inversely on the closeness to resonance. The wire that generated the dyeline is marked with a +. The dye particles will be initially displaced from the wire during the impulsive tilt-out that began the forcing. After this initial displacement (which will be a slight curve since 0.1 s is about 1/6 of a rotation period and the Coriolis force will have time to act) the particles will start to trace out an orbit with a radius appropriate to the forced amplitude.

If the orbits were circular, and centred on the wire, the displacements of the dye particles from the wire, projected onto the plane viewed by the camera, would be perfectly constant, because the time dependence of their orbital motion is perfectly cancelled by that of the camera. However, even a circular orbit would not be centred on the wire. There are at least three reasons for this, under linear inviscid theory alone. Firstly, the forced-motion orbit's 'centre' is not at the wire; as shown in figure 2, the steady orbital trajectory passes close to the wire since the particles start off there. Secondly, superimposed on the forced motion is the transient response, or free-mode 'ringing', whose amplitude depends only on the magnitude of the initial tilt-out. The free mode with the largest amplitude is the one with the spatial structure closest to the form of the initial disturbance, namely the (1,1,1) mode. Thus this largest free mode response closely resembles the forced response in structure; also, it oscillates with a natural frequency which is close to the forcing frequency, because the (1,1,1) mode is being forced near resonance. Thirdly, as with the surface gravity wave paradigm, there is a 'Stokes drift' of the orbits. Because of the linear solution's three-dimensional velocity field (sinusoidal and Bessel functions) a particle finds itself in a slightly different part of the velocity field on the completion of each orbit. (For simplicity, the free-modal response and 'Stokes drift' are not shown on figure 2.)

Nevertheless, on the plane imaged by the camera fixed on the turntable, the displacement of the dyeline from on the wire should not appear to reverse sign in an oscillatory fashion. This is because, as noted above, the oscillatory time dependence of the dye particles in tank coordinates is precisely the same as that of the imaged plane; the camera in effect 'follows' the dye particles around on their orbits.

The residual apparent motion of the dye particles relative to the wire on the imaged plane should be that due to the eccentricity of the orbit centres due to the initial displacement, the beating between the forced and free modes and the 'Stokes drift'. All these influences, as well as the 'radius' of the orbit (which is steady once a steady forcing regime is established), are ultimately related to the forced mode amplitudes (or directly to the size of the initial tilt, upon which the forced mode amplitudes depend). Thus the distance, $\Delta(z)$, of the dyeline from the wire, projected onto an (r, z)-plane

(a)

Tank
rotation

8 1 2

7

3

6

5 4

Camera

• Particle

+ Wire

(b)

Tank
rotation

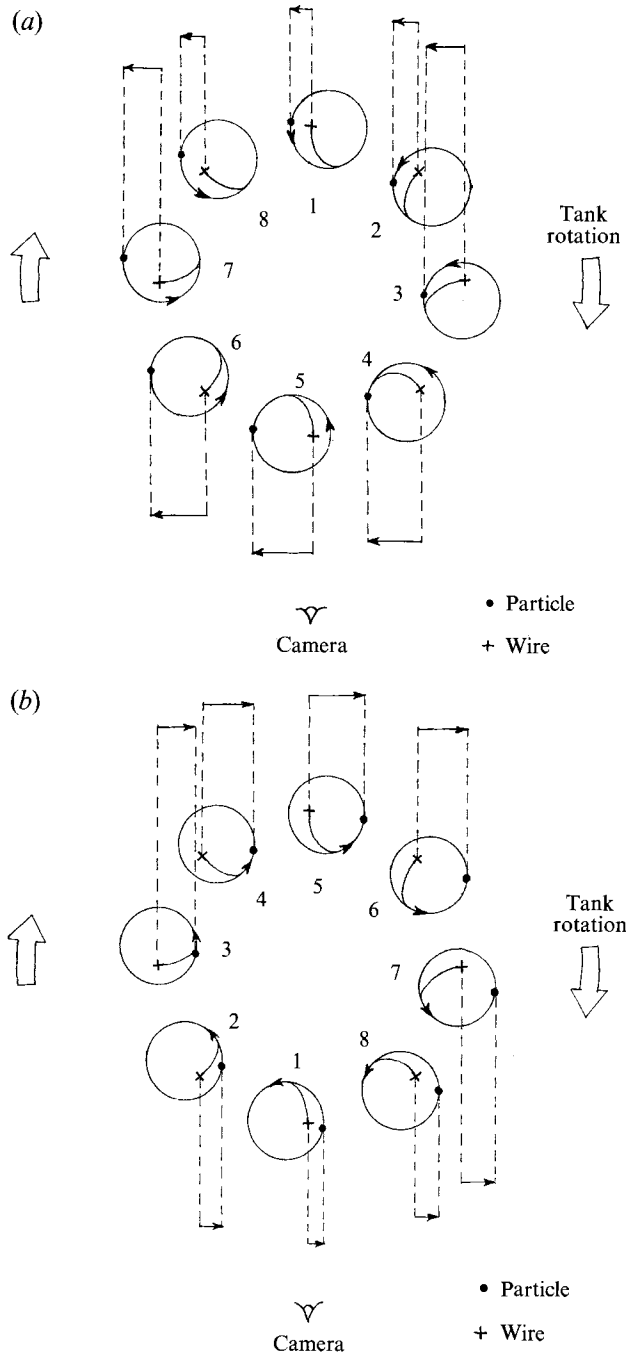4 5 6

3

7

2 8

1

Camera

• Particle

+ Wire

FIGURE 2. Motion of dye particles under the influence of forced inertial modes. The diagram shows dye particle displacements $\Delta_p(z)$ for a particular z, projected onto the plane imaged by the camera in the turntable or precessing frame of reference, from which the exposures (figure 5a–h) were taken. The tank, viewed from above, is rotating clockwise in this frame of reference. Orbits of the particles, shown for simplicity as circular, without the influence of free modes and neglecting Stokes drift, are drawn at eight positions relative to the turntable-fixed camera. The horizontal arrows show Δ_p. (a) View of particles near the top of the tank, which initially tilts away from the camera, thus the initial displacement (at position 1) relative to the wire is towards to camera; Δ_p is to the left. (b) View of particles near the bottom of the tank, which initially tilts towards the camera; the initial displacement (position 1, noting that base of the wire at the bottom is almost diametrically opposite its base at the top) is away from the camera; Δ_p is to the right.

fixed in *turntable* coordinates (where it is called $\Delta_p(z)$) will ultimately depend on $\sum_{n=1}^{\infty} A_n$, where A_n is the amplitude of each mode. However, the dependence will not be simple because of the complicating kinematic factors just mentioned. Near resonance of a low-order mode, that mode should dominate the sum. It is possible to estimate $\Delta(z)$ from $\Delta_p(z)$, and hence get a measure characteristic of what we presume to be A_n, where n is the index of the low-order mode near resonance, to within about $\pm 50\%$, by viewing the video recordings of the spinning tank.

From §2 the axial structure of the flow field near the resonance of a low-order mode should be sinusoidal with argument $k\pi(z/h + \frac{1}{2})$, and hence $\Delta(z)$ will have this dependence on z. From the point of view of the camera (a side view in the turntable frame), the dyeline should initially appear to tilt, as the fluid particles are displaced relative to the tank by its initial tilt-over and by the resulting Coriolis acceleration. This tilt should be modified by the free and forced modes of oscillation; when, as in the experiments to be described, these modes are dominated by the (1,1,1) mode, the tilt should appear as one-half of a sine wave with a zero at the tank centroid.

5. Calculations of dyeline displacement based on linear inviscid theory

Linear inviscid calculations were made (summarized in the Appendix to this paper and detailed in Manasseh 1991), which permit an accurate prediction of the forced response to be made. Precise comparisons of a predicted linear flow field with these experiments are not possible, for two reasons. First, the rough nature of the estimation of the experimental response, with its associated uncertainty of about $\pm 50\%$, precludes a precise comparison and probably befits best a scale comparison, which will be given in §6. Secondly, the comparison must be made on the basis of a few seconds' observation – within a few revolutions of the commencement of forcing – since the flow appears to irreversibly distort after this time. Despite these caveats, a numerical calculation of the dyeline displacement is still useful because it serves to highlight both the initial similarities and the later differences that develop between the structure of the predicted linear inviscid response and that in the actual experiment.

The basis of the calculation is an integration of the ordinary differential equations (2.11) for the forced fluid velocity, giving the path of a passive tracer particle under the influence of inertia wave modes. Several particles are started along the actual coordinates of the wire in the tank, and their positions at successive one-revolution periods are joined to form a simulation of the dyeline seen in the experiment.

The time taken for the initial tilt was about 0.1 s. The actual mechanical arrangement causing the tilt-out was a spring with a pneumatic damper. The damper was adjusted so that the motion was just underdamped; it reached the preset θ without any overshoot or jarring. Thus this brief tilting motion is modelled by the first quarter-period of a sine function that reaches its peak at 0.1 s.

The calculation also incorporates some reckoning of the transient response, or free-mode 'ringing', due to the initial impulse that sets up the forcing. (In inviscid theory this ringing continues forever, but since only a tenth or so of the viscous decay timescale is being considered, an inviscid model seems appropriate for the free-mode response.) The precise value of the initial impulse given in the experiment could not be measured and could only be roughly inferred from the calibrations in Manasseh (1991). Further details are in the Appendix.

The predicted dyeline displacement is shown in figure 3. Although the calculation and plot are in tank coordinates, the orientation of the wire has been chosen to

approximate its instantaneous orientation in the earliest experimental photographs reproduced in §6.

The first 'dyeline' plotted is the locus of particle displacements at the first one-half period after the initial tilt; at this time and after successive one-period intervals the particles appear close to their maximum projected displacements for the chosen orientation, making it easier to discern the axial flow structure. Further details on the calculation are in the Appendix. In figure 4, we have 'zoomed-in' on figure 3 to make individual pathlines more clear. In these end-view projections only the topmost pathline has been plotted. From this viewpoint the particles are moving anticlockwise on their orbital paths. The advective drift or 'Stokes drift' can be noted in these end-view projections.

6. Experiments

Initial trials were conducted with $\theta = 1°$ and near the (1,1,1) mode resonance, to study the behaviour of the thymol dyeline. It was generated as part of the computer-controlled experimental sequence. These trials determined that nutation angles greater than $\theta = 1°$ forced the system with too large an amplitude for the dyeline technique to be of much use; the fluid response was sufficient to sweep the dye away from the wire before it had a chance to form a dyeline. Furthermore, if the forcing frequency was too close to a resonance, dye was swept away from the wire even before the experiment could begin, since there was always some small non-zero θ because of unavoidable inaccuracies in the equipment. The trials were conducted near the resonant frequency of the (1,1,1) mode, $\omega = 2.64298$, and established the working range, $2.40 < \omega \lesssim 2.55$, of ω values near the (1,1,1) mode resonance over which the thymol dyeline technique could be used to observe the forced behaviour beyond a few revolutions. Presumably, equally good visualizations would have been obtained with frequencies equally far above the resonant peak as the lower limit of the working range is below it; however it was not practical to operate the apparatus at the very highest such speeds. Some experiments were run at $\omega = 2.74$ and $\omega = 2.78$ but it was judged unsafe to conduct a lengthy series of experiments at the corresponding speeds.

Experiments in this working range were then performed in order to address the aims of §1. A series of experiments was conducted at $\omega = 2.46$, 2.5, 2.54, 2.74 and 2.78. The nutation angle was set at $\theta = 1°$. There were four runs at each ω with identical settings. A more detailed survey of the parameter space near this (1,1,1) mode resonance had been planned. However, it turned out that the richness of the phenomena observed for this limited number of points in parameter space meant that the observation and description of much more data would have been an overwhelming task.

The dominant feature of all the dyeline experiments is the rapid development of structures that cannot be described by the linear inviscid theory of §2. Further experiments were conducted near the (3,1,1) and (5,2,1) mode resonances, which it is hoped will be presented in a future paper. With the (5,2,1) mode in particular it is hard to select any features that seem compatible with a linear inviscid response. Nevertheless, at early times after the commencement of forcing near the (1,1,1) mode resonance, the time dependence and structure of the dyeline displacement seem to be consistent with a linear inviscid description.

Therefore, estimates were made of the displacement $\Delta(z)$, near the tank ends $z = \pm h/2$ where $\Delta(z)$ is initially a maximum. This was thought to be characteristic of the amplitude of what was postulated to be the (1,1,1) mode under linear inviscid
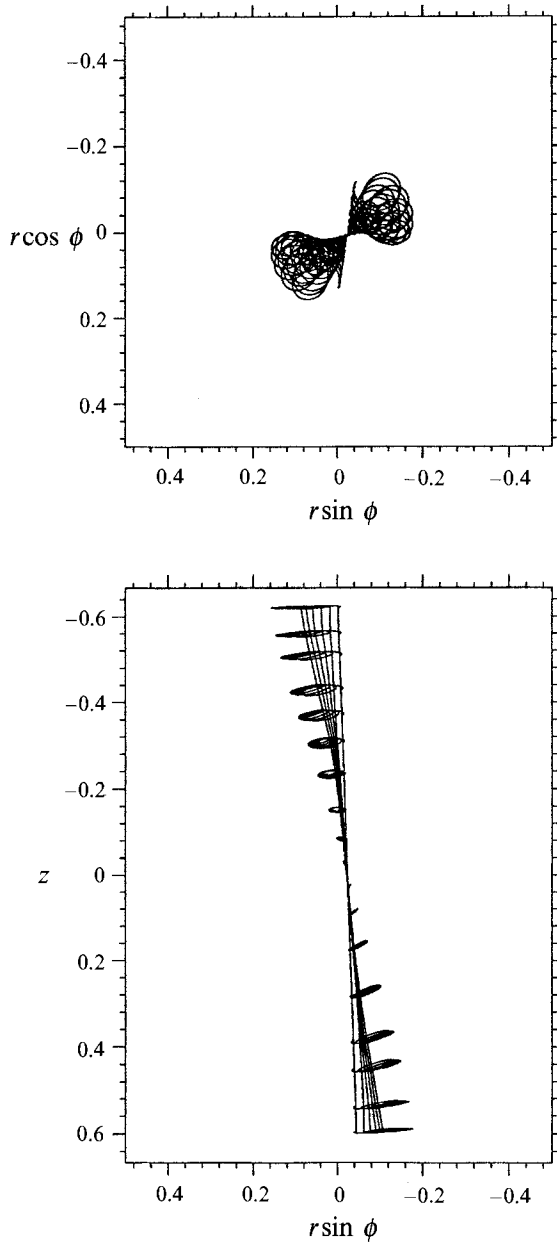
FIGURE 3. Side and end views of the pathlines. The pathlines are relative to container-fixed coordinates; however, on the side-view plot, particles have been joined at each revolution to give an impression of the dyeline shape when viewed from the turntable, and the plot has been rotated to give approximately the same phase of the wire as in the earliest experimental photographs – hence the reversed sense of the coordinates. The first dyeline is at $t = 0.5$ revolutions, to match the estimated time of the first photograph, figure 5(a). The actual coordinates of the experimental wire have been used; slight departures from symmetry of the pathlines in the top and bottom halves of the tank are due to the wire not passing through the tank centroid, owing to experimental constraints.
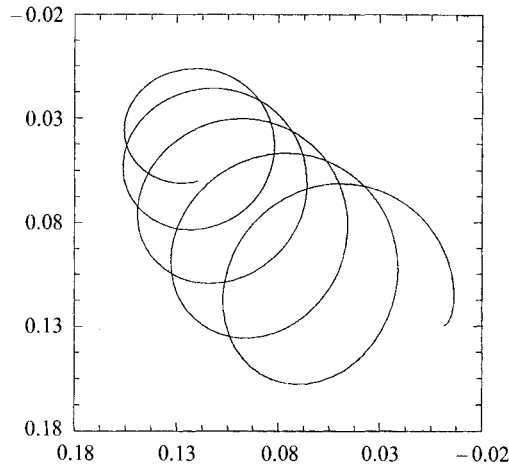
FIGURE 4. Expanded view of one of the pathlines looking from the end of the cylinder. The pathline shown is the topmost one in figure 3. As in figure 3, the reversed sense of the coordinates is due to the rotation of the plot to give approximately the same phase of the wire as in the earliest experimental photographs.

theory. The estimate was made in the first few revolutions after the commencement of forcing, from the experiments recorded at $\omega = 2.46, 2.50$ and 2.78 . There was considerable uncertainty in which time, if any, was the correct one at which to make these estimates. After a few revolutions the structure begins to irreversibly distort, and during this brief time it is hard to say if there is a steady displacement of the dyeline from the wire. Owing to this uncertainty the error in estimating the dyeline displacement at this early stage was about ± 2 mm, about 50%. Estimates were also made from the initial trials at $\omega = 2.6$, before the dyeline at this frequency became too faint to be discerned. The best visualizations were obtained at $\omega = 2.46$.

The behaviour at $\omega = 2.46$ is illustrated by photographs, figure 5(*a–h*). Here, the microcomputer controlling the experiment was programmed to take an exposure every revolution, beginning immediately after the impulsive tilt. The uncertainty in the time $t = 0$, caused by human error in simultaneously initiating the tilt and microcomputer sequence, is about ± 0.3 s (± 0.5 revolutions). The first photograph was therefore at $t = 0 \pm 0.3$ s or $t = 0 \pm 0.5$ revolutions. The phase of the wire relative to the camera at the commencement of forcing is random.

After the commencement of forcing, the dyeline moves away from the wire, initially appearing like a straight line but tilted away from the wire at the tank top and bottom. This state is shown in figure 5(*a*), taken immediately after the commencement of forcing at $t = 0$. (It is probable, given the extent of development of the dyeline displacement in this first photograph, that it was taken close to the $t = +0.5$ revolution limit of the error band $t = 0 \pm 0.5$ revolution.) As noted in §4, the dyeline tilt is due to a combination of the displacement of the fluid following the impulse that initiated the forcing, the displacement due to the Coriolis acceleration during the time the impulsive motion was occurring and the displacements caused by the forced and free modes of oscillation and the 'Stokes drift'.
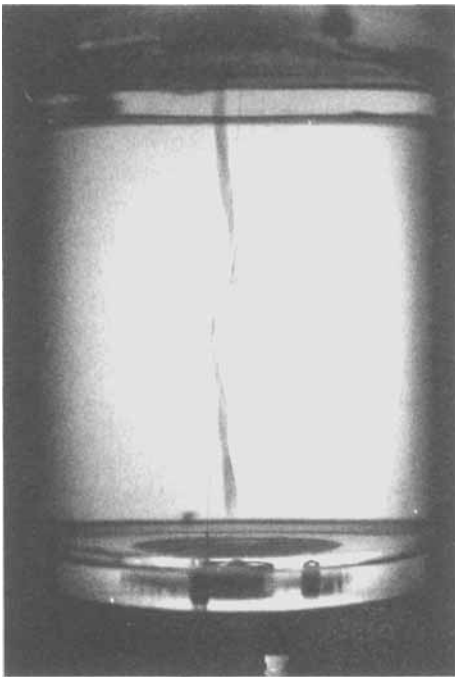
In the images of figure 5(*a–h*), the top of the tank and the wire fixed to it have been tilted away from the camera (and the bottom towards it). The dyeline is thus displaced from the wire towards the camera in the top half of the tank (and away from the camera in the bottom half). Since the camera continues to rotate from left
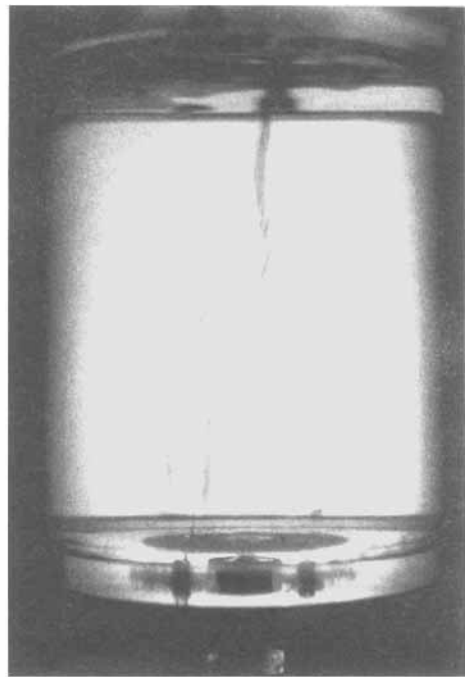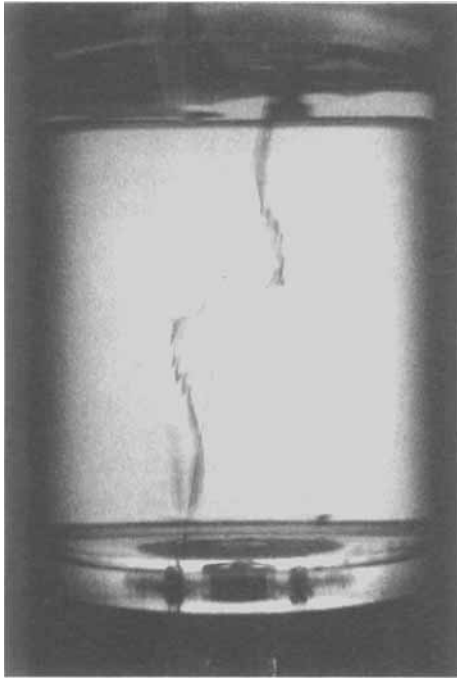
R. Manasseh
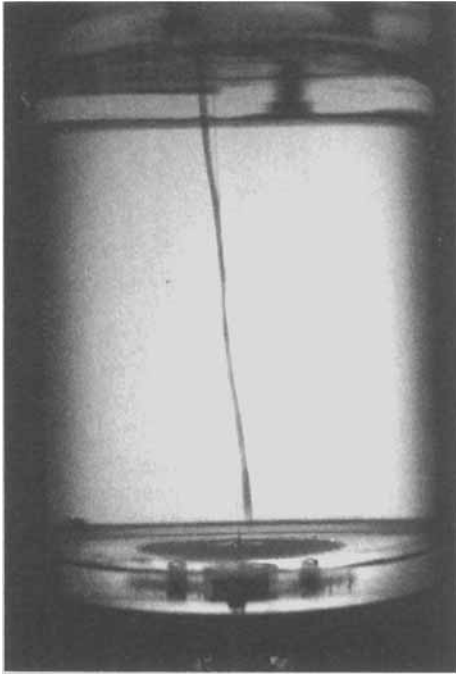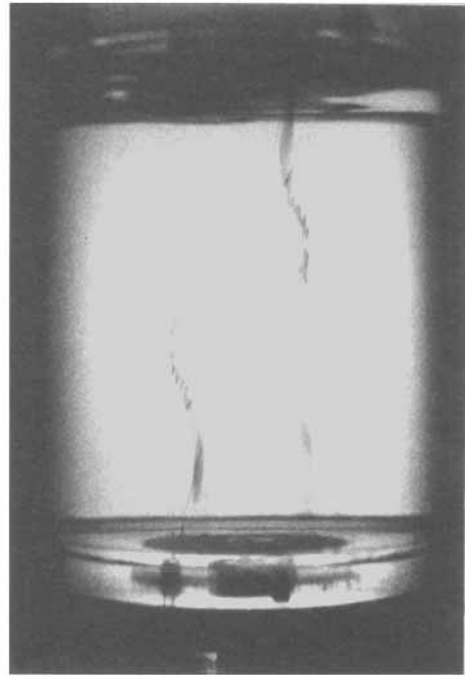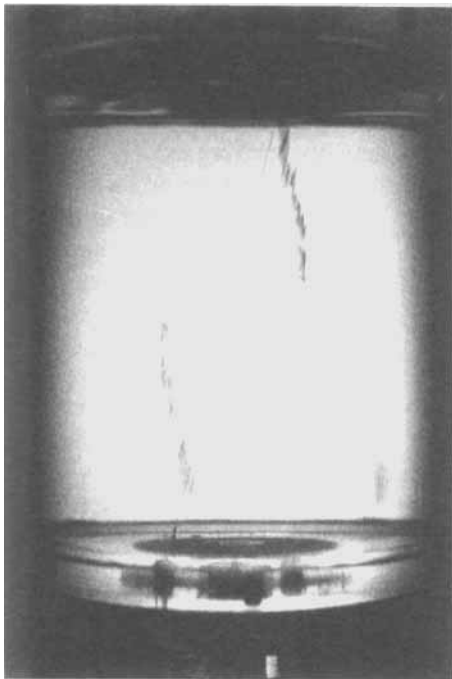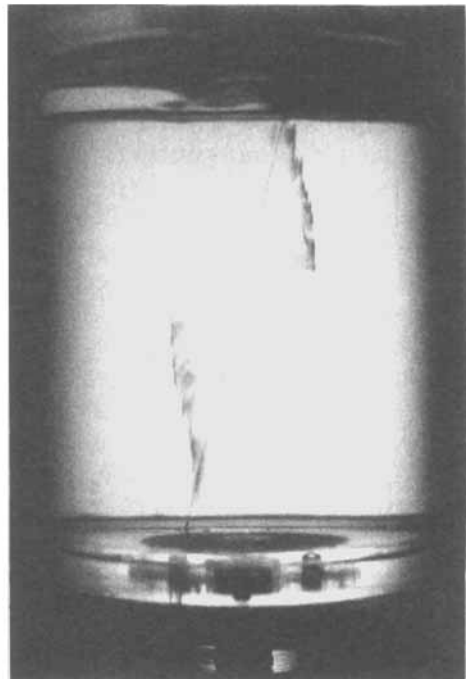

(a)
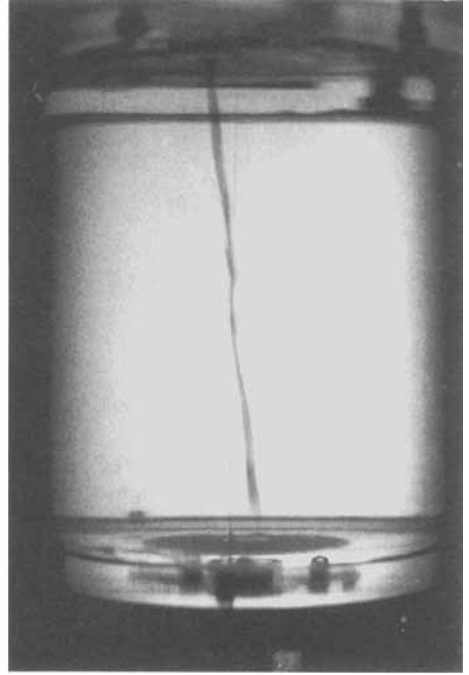
(b)

(c)

(d)

FIGURE 5 (a–d). For caption see facing page.

(e)

(f)

(g)

(h)

FIGURE 5 (*a*–*h*). Dyeline experiment, $\theta = 1°$, $\omega = 2.46$. The spinning tank is being viewed from the turntable: (*a*) was taken at about 0.5 revolutions after the impulsive tilt, the remainder at approximately 2 revolution intervals. (The exposures were taken approximately every revolution; every second exposure has been reproduced here.) Slight shifts in phase of the wire are due to inaccuracies in the timing of the camera's motor drive. A dark vertical stripe near the tank bottom in some photographs is a shadow from a small internal crack in the tank wall.

to right relative to the tank, the dyeline always appears to tilt to the left in the top half of the tank (and to the right in the bottom half), as suggested schematically by figure 2. The net displacement does seem to be one-half of a sine wave with a zero at the tank centroid. Moreover, the displacement of the dyeline relative to the wire at this stage does not reverse sign (nor show any discernable oscillation) in the turntable (camera) frame of reference, since as expected it has the same frequency as the forcing. Thus the initial observation is consistent with the linear response dominated by the (1,1,1) mode predicted in §4.

It was at this early stage that the estimates of the amplitude were made, by viewing video recordings. The tilted dyeline corresponds to the dyeline particles tracing out roughly circular trajectories in tank coordinates, at $-\omega_1$, opposite to the frequency of the tank relative to the turntable, ω_1, with maxima in the dimensions of the orbits near the tank ends. From the video recordings (see the earliest datapoints in figure 6, which will be described later), the dimension $\Delta(z)$ of these orbits at $\omega = 2.46$ is about 4 ± 2 mm near the tank ends $z = \pm h/2$ where the maximum azimuthal and radial velocities should occur and do appear to occur initially. From this dimension, assumed, from the argument in §4, to be characteristic of the orbit diameter, the fluid velocity can be estimated. The orbital path length is about $\pi \times 4 \pm 2$ mm $\approx 12 \pm 6$ mm. The velocity of fluid particles is therefore $\omega_1 \times 12 \pm 6$ mm $\approx 20 \pm 10$ mm s^{-1}. This velocity is consistent with the scale assumed under linear behaviour, which gives $U = \omega_1 D\theta \approx 16$ mm s^{-1}.

A periodic variation in the displacement of the dyeline from the wire could not be confidently discerned. Recall, from §4, that this variation is due to the eccentricity of the orbit centres owing to the initial displacement, the beating between the forced and free modes and the 'Stokes drift'. Measurements (shown in figure 6) were made from the video images of the dyeline displacement (which is Δ_p, Δ projected onto the imaged plane) at half-revolution intervals. However, the developing instability about to be described begins after a few revolutions, precluding any statistical confidence in the couple of measurements that may be in the linear inviscid regime.

In the experiments no systematic change in amplitude was observed, within the estimation error of about $\pm 50\%$, at each of $\omega = 2.5$, 2.60, $\omega = 2.78$ and at $\omega = 2.46$.

In the experiments, the dyeline does not remain approximately fixed in shape as predicted by linear inviscid theory and as illustrated by numerical calculations based on such theory. Figures 5(b)–5(h) show the later development; they are at 2 revolution intervals, with figure 5(b) being at about 2.5 revolutions and figure 5(h) at about 14.5 revolutions. After about 5 revolutions (3 s in real time), a 'kink' begins to develop in the dyeline which, in the course of the next few revolutions, develops into an 'S' shape, i.e. a function that is odd in z with an axial wavenumber of approximately 3/2. This 'kink' of the dyeline away from the wire at the tank centreplane is where linear inviscid theory predicts the minimum displacement. In addition, this new 'kink' structure rotates with the tank, and hence is non-oscillatory in tank coordinates. This is in contrast to the linear-theoretical response, which should appear approximately steady in the turntable (forcing) frame of reference since it is oscillatory in tank coordinates. The video recordings clearly show that the new development becomes three-dimensional, resembling two half-turns of a corkscrew. By 14.5 revolutions (figure 5 h) the upper and lower arms of the dyeline have wound up into spiral forms. All the details described above seem to be perfectly repeatable.

In figure 6 measurements are shown of the displacement of the dyeline from the wire, at half-revolution intervals. After about 5 revolutions (3 s) the measured displacements on either side of the tank diverge, owing to the enticement of the dye
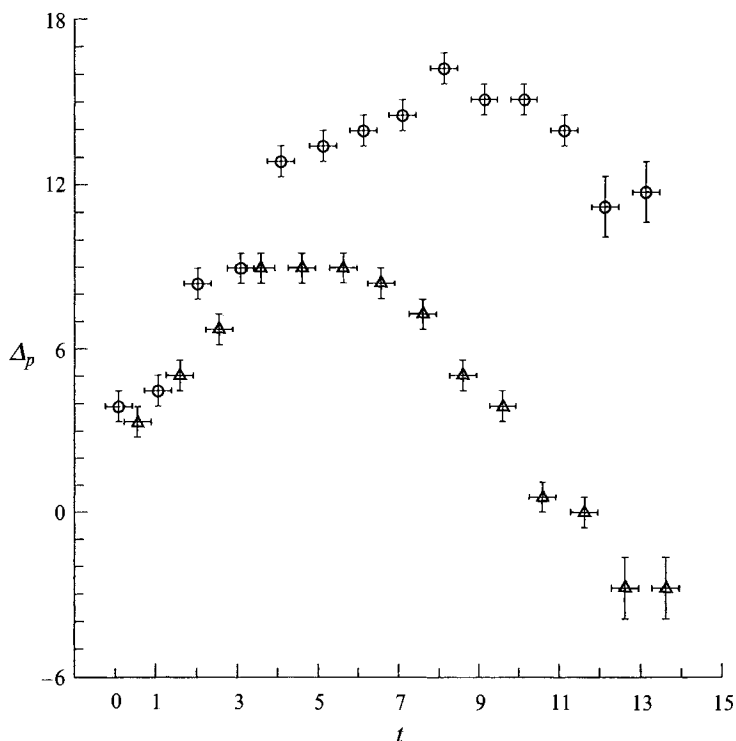
FIGURE 6. Projected displacement Δ_p (in mm) of the dye from the wire, measured from the video images, for $\theta = 1°$, $\omega = 2.46$, as a function of time t (in revolutions). The measurements were made relative to the wire near the bottom of the tank (at $z = 0.6$), hence, in the first few revolutions, the dye particles are displaced to the right (positive Δ_p), as shown in figure 2(b). $\triangle$: the displacement to the furthest discernable limit of the dyeline, when the wire is on the right of the image, and $\circ$: on the left. The measurements have not been corrected for optical distortion from the circular tank wall or the video screen.

into the new non-oscillatory 'kink flow' that can be observed developing from this time. If the motion had remained according to linear inviscid theory, the datapoints from the left- and right-hand sides would each have followed a straight line at constant Δ_p, modulated by a beating with the free modes and the Stokes drift.

The velocity of fluid displacement causing the kink is an initial maximum of ~ 4 mm s^{-1}, since it reaches a radius of about $r = 0.25$ (22 mm) in about 10 revolutions (6 s). This should be compared with about ~ 20 mm s^{-1} for the oscillatory modal response. The non-oscillatory motion of the kink does not imply that all oscillatory motion in the tank has ceased, rather that a non-oscillatory flow (which is able to cause a net transport of dye) has arisen in addition to the oscillatory flow. The flow causing the kink appears to arrest after about 10 revolutions, when the more complicated 'winding up' of the dyeline arms is noted.

This 'winding up' appearance can be traced to striations in the dyelines, first visible in figure 5(d), which begin near the centre of the tank. It is in this region where the fluid velocities are smallest under linear inviscid theory, being zero at the centroid. If an influence from the wire were to generate the striations (by vortex shedding for example) this would be expected to be in a region where velocities are more substantial. Furthermore, an influence from the wire would be expected to manifest itself first where flows are closer to normal to the wire, where the wire presents more

of an obstacle. The regions of the tank where flows are close to normal to the wire are at the ends of the tank. Again this is away from the centre where the striations are first seen.

The axial nature of the striations, or 'winding-up' appearance of the dyelines, is noteworthy, as is the spread of these small-scale features throughout the tank. Possibly they represent the spread of turbulent eddies as the flow becomes more disordered. Eddies in rotating flows would be expected to exhibit a strong axial orientation. The 'Type B' breakdown (Manasseh 1992) that occurs for the parameters of the present experiments is characterized in part by small-scale axially oriented features.

Although the kink is a visually dramatic departure from the linear inviscid description, it should be remembered that its velocity is at most 20% of the linear response. Structures like the kink were not noted by McEwan (1970) and Manasseh (1992). This can be ascribed to the nature of the reflective flake visualization technique they used. As the spatial gradients in the 'kink flow' and the (1,1,1) mode flow appear similar, we can infer that their strain fields, which align the reflective flakes, are in the same approximate ratio as their velocity fields, i.e. about $1/5$. The kink was probably not noted because it corresponds to a weak strain distribution rotating with the tank. Any such strain distribution will only be noted as it passes through the sheet of light (see Manasseh 1992 for details) illuminating a reflective flake experiment. Unless the kink is really a manifestation of a perfectly axisymmetric flow, it should appear as a weak flickering of the reflected image, with a frequency equal to the rotation rate of the tank relative to the turntable (or to some multiple of it, if the kink structure has many radial planes of symmetry). Moreover, as the 'kink flow' arrests after about 10 revolutions, its strain distribution should appear as a weak flickering that persists for only about 10 revolutions, perhaps explaining why it was not noted in McEwan (1970) or Manasseh (1992).

Experiments previously conducted in the current working range, with the reflective flake visualization technique (Manasseh 1992), had determined that the typical breakdown expected for $2.40 < \omega < 2.50$ was a long-timescale instability manifesting itself in the order of 100 revolutions. For $2.50 < \omega < 2.55$ Type B collapses occur, again in the order of 100 revolutions. At $\omega = 2.60$ a Type A collapse was noted to occur in the order of 50 revolutions. Type A collapses result in the generation of turbulence with eddy scales about a tenth of the tank diameter, whereas Type B collapses result in a weakly turbulent flow and appear to be preceded by interactions with higher-order modes. The dyelines generated at $\omega = 2.46$ had dissipated by about 50 revolutions after the commencement of forcing, making further visualization impossible; dyelines generated at $\omega = 2.60$ had dissipated by about 10 revolutions. Therefore, in these dyeline experiments, the dyelines had dissipated before the 'resonant collapse' instability as identified by the reflective flake technique had manifested itself.

It was not possible to generate dyelines at later stages during the experimental run, because, as noted in §3.2, a period of about 60 seconds without any flow was needed to generate a dyeline. Had the current been switched on when flow was being forced, dye would have been swept away from the wire too rapidly for a dyeline to be formed.

The repeatablilty of the kink formation raises the possibility that it is wholly or in part associated with some geometric feature of the tank, the forcing regime or with a systematic fault in the experiment. It was in part to address this concern that further experiments were done with higher modes, to see if the kink still occurs at other forcing frequencies. It does not; for the (3,1,1) mode, for example, equal departures from the linear inviscid prediction begin at three points, corresponding exactly to the

intersection of the axis with the three 'nodal planes' where velocities normal to the axis are identically zero according to the linear theory for the (3,1,1) mode. (In fact, the (1,1,1)-mode kink occurs at the single nodal plane of the (1,1,1) mode.) More complex structures occur for still higher modes, without the presence of a clear kink as with the (1,1,1) mode. As with the (1,1,1)-mode results, these observations are easily repeatable.

The fact that quite different anomalies arise at different forcing frequencies (with the tank geometry and the amplitude and structure of the forcing function identical) suggests that the kink does not arise from a geometric flaw or some fault in the experimental procedure. It is hoped that experiments with other modes will be reported in a future paper.

7. Discussion and conclusion

The primary aim of this series of experiments was to examine the dyeline pattern before a breakdown had occurred and to see if it is consistent with the predictions of linear inviscid theory. It is, albeit for only a few revolutions; a measure characteristic of the flow amplitude has the correct scale and the time dependence is oscillatory in tank coordinates as expected. However, a 'kink' soon develops in the linear inviscid dyeline structure. It is a manifestation of a flow that is not oscillatory and has a velocity about 1/5 of the estimated linear component of the response.

It is conceivable that the kink in the dyeline originates in the viscous terms neglected in the simple analysis of §2, either in an Ekman or Stewartson layer effect or even in some interaction with the visualization wire itself. Also, discontinuities on characteristic surfaces are predicted in contained rotating fluids (Wood 1966) which may have a physical realization as extensions of the viscous boundary layers into the interior. If viscous forces are at work, we expect the flows they represent to be of $O(E^{\frac{1}{2}})$ times the first-order inviscid amplitude. This is about 3×10^{-3} times the first-order inviscid amplitude. For the experiment in §6 a measure characteristic of this amplitude was estimated to be about 20 mm s^{-1}, giving viscous flows of order 10^{-2} mm s^{-1}. However, the flow that produced the kink in figure 5(e) had a magnitude of order 1 mm s^{-1}. This is one and a half to two orders of magnitude larger than a viscous mechanism would predict. There are not enough precise data to rule out a viscous mechanism for producing the kink, but on the basis of its order of magnitude that seems an improbable cause.

A secondary aim was to determine if a large mean flow (corresponding, say, to a circulation of order 0.1 times the basic spin ω_1 as suggested by Gunn & Aldridge 1990) was present. However, even the small mean flow calculated by Thompson (1970) was not observed. This is now to be expected as it is $O(\theta)$ times the first-order forced response amplitude, and since a measure characteristic of this amplitude is about 20 mm s^{-1}, the second-order mean flow should be about 0.2 mm s^{-1}. Thus over the 5 revolutions or so before the kink appeared, about 3 s in real time, the dyeline would only have moved about 0.6 mm, a distance too small to be clearly distinguished from the flow due to the first-order forced response. It was not possible to generate a first-order forced response sufficiently large for a noticeable second-order flow to develop.

In conclusion, the use of the dyeline technique has suggested that linear inviscid theory for contained inertia waves has some validity, for a very brief period following the commencement of forcing, both in its prediction of the scale of flow velocity and of the flow's oscillatory time dependence. However the experiments have also

revealed the formation of a structure not explained by linear theory, which develops before the collapses detailed in Manasseh (1992), indeed within a few revolutions of the commencement of forcing.

A mean circulation could be invoked to explain this or other breakdown phenomena. However, some mechanism is needed to explain how a mean circulation can interact with the inertia wave modes, and grow larger than the second-order level permitted by formal asymptotic theory (Thompson 1970).

Further experiments were carried out to test ideas that the 'kink' originated in a weakly nonlinear interaction with a mode that cannot be forced under linear theory. It is hoped that these, along with the results of experiments near the resonances of higher-order modes and further discussion and speculation on the nature of these instabilities will be presented in future papers.

Appendix.   Calculations of the dyeline displacement

A.1.   *Forced response calculation*

First, it is shown how the linear steady-state velocity field resulting from an applied, single-frequency forcing can be estimated by summing a series of inertia wave modes, with their amplitudes calculated by a 'mode projection' approach. A mode projection approach to calculating the amplitudes of forced inertial oscillations in a cylinder was first described in the unpublished thesis of Kudlick (1966), though numerical calculations based on it were not required for comparisons with experiment. This approach can be contrasted with the 'inhomogeneous boundary condition' method, which expresses the disturbance pressure as a Fourier series in z, from which the velocity field can be derived. It is detailed in Tan (1991). In the mode projection approach, the projection of the applied force field onto a particular mode is calculated. Each of these modes individually satisfies the homogeneous boundary conditions. Then the responses or projections of all possible modes, when appropriately recombined, should reproduce the force field. Although mathematically standard and straightforward, as detailed in Manasseh (1991), neither approach, when realized numerically, is without its pitfalls; the difficulties may be related to the ill-posedness of the original problem defined by (2.2) and (2.3).

Secondly, the free mode response is estimated, based on the measurements of the initial impulse in Manasseh (1991), and the velocity field is integrated to determine a number of particle paths.

To begin a calculation based on the mode projection approach, first establish some identities by considering once more the homogeneous form of (2.2),

$$\frac{\partial \boldsymbol{u}}{\partial t} + \omega \hat{\boldsymbol{k}} \times \boldsymbol{u} + \nabla p = 0, \tag{A 1}$$

with incompressibility and the homogeneous boundary condition $\boldsymbol{u} \cdot \hat{\boldsymbol{n}} = 0$, where $\hat{\boldsymbol{n}}$ is the outward unit vector normal to the surface. For special values of ω, say ω_n, (A 1) is satisfied with a single mode of the form

$$\boldsymbol{u} = \mathrm{Re}\left(\boldsymbol{U}_n(r, \phi, z)\, \mathrm{e}^{\mathrm{i}t}\right), \tag{A 2}$$

$$p = \mathrm{Re}\left(Q_n(r, \phi, z)\, \mathrm{e}^{\mathrm{i}t}\right), \tag{A 3}$$

where n corresponds to a combination of spatial wavenumbers that is unique to each mode. Then (A 1) becomes

$$\mathrm{i}\boldsymbol{U}_n + \omega_n \hat{\boldsymbol{k}} \times \boldsymbol{U}_n + \nabla Q_n = 0. \tag{A 4}$$

Following Greenspan (1968) we can arrange the following expressions from (A 4), where n_1 and n_2 represent different modes:

$$\mathrm{i}\boldsymbol{U}_{n_1} \cdot \boldsymbol{U}_{n_2}^{\dagger} + \omega_{n_1}(\hat{\boldsymbol{k}} \times \boldsymbol{U}_{n_1}) \cdot \boldsymbol{U}_{n_2}^{\dagger} + \nabla Q_{n_1} \cdot \boldsymbol{U}_{n_2}^{\dagger} = 0, \tag{A 5}$$

$$-\mathrm{i}\boldsymbol{U}_{n_1} \cdot \boldsymbol{U}_{n_2}^{\dagger} + \omega_{n_2}\boldsymbol{U}_{n_1} \cdot (\hat{\boldsymbol{k}} \times \boldsymbol{U}_{n_2}^{\dagger}) + \boldsymbol{U}_{n_1} \cdot \nabla Q_{n_2}^{\dagger} = 0, \tag{A 6}$$

where $\dagger$ denotes complex conjugation. Now consider the integrals of (A 5) and (A 6) over the container volume. First note that

$$\nabla(Q_{n_1} \cdot \boldsymbol{U}_{n_2}^{\dagger}) = \nabla Q_{n_1} \cdot \boldsymbol{U}_{n_2}^{\dagger}, \tag{A 7}$$

because of the incompressibility condition. Then

$$\int_{\mathscr{V}} \nabla Q_{n_1} \cdot \boldsymbol{U}_{n_2}^{\dagger}\, \mathrm{d}\mathscr{V} = Q_{n_1}\int_{\mathscr{S}} \boldsymbol{U}_{n_2}^{\dagger} \cdot \hat{\boldsymbol{n}}\, \mathrm{d}\mathscr{S}, \tag{A 8}$$

by Gauss's theorem, where $\mathscr{V}$ is the container volume and $\mathscr{S}$ is its surface. Then, because of the boundary condition,

$$\int_{\mathscr{V}} \nabla Q_{n_1} \cdot \boldsymbol{U}_{n_2}^{\dagger}\, \mathrm{d}\mathscr{V} = 0, \quad \forall\ n_1, n_2. \tag{A 9}$$

As

$$\boldsymbol{U}_{n_1} \cdot (\hat{\boldsymbol{k}} \times \boldsymbol{U}_{n_2}^{\dagger}) = -(\hat{\boldsymbol{k}} \times \boldsymbol{U}_{n_1}) \cdot \boldsymbol{U}_{n_2}^{\dagger}, \tag{A 10}$$

integrating (A 5) and (A 6) over the volume and adding them gives

$$(\omega_{n_1} - \omega_{n_2})\int_{\mathscr{V}} (\hat{\boldsymbol{k}} \times \boldsymbol{U}_{n_1}) \cdot \boldsymbol{U}_{n_2}^{\dagger}\, \mathrm{d}\mathscr{V} = 0, \tag{A 11}$$

so that

$$\int_{\mathscr{V}} (\hat{\boldsymbol{k}} \times \boldsymbol{U}_{n_1}) \cdot \boldsymbol{U}_{n_2}^{\dagger}\, \mathrm{d}\mathscr{V} = 0, \quad n_1 \neq n_2, \tag{A 12}$$

and therefore, from the integral of (A 5) and from (A 9),

$$\int_{\mathscr{V}} \boldsymbol{U}_{n_1} \cdot \boldsymbol{U}_{n_2}^{\dagger}\, \mathrm{d}\mathscr{V} = 0, \quad n_1 \neq n_2, \tag{A 13}$$

i.e. the functions $\boldsymbol{U}_n$ must be orthogonal. Now define the inner product operation as

$$\langle \boldsymbol{X}, \boldsymbol{U}_n \rangle = \int_{\mathscr{V}} \boldsymbol{X} \cdot \boldsymbol{U}_n^{\dagger}\, \mathrm{d}\mathscr{V}, \tag{A 14}$$

where $\boldsymbol{X}$ is any complex vector function of r, ϕ and z. Applying this operation to (A 4) gives

$$\mathrm{i}\langle \boldsymbol{U}_n, \boldsymbol{U}_n \rangle + \omega_n\langle \hat{\boldsymbol{k}} \times \boldsymbol{U}_n, \boldsymbol{U}_n \rangle = 0, \tag{A 15}$$

because of (A 9), (A 12) and (A 13). Hence

$$\frac{\langle \hat{k} \times U_n, U_n \rangle}{\langle U_n, U_n \rangle} = -i\frac{1}{\omega_n}. \tag{A 16}$$

Now consider the inhomogeneous problem

$$\frac{\partial u}{\partial t} + \omega \hat{k} \times u + \nabla p = \text{Re}\left(F\, e^{it}\right), \tag{A 17}$$

where ω is prescribed and does not coincide with any of the ω_n, together with incompressibility and boundary conditions. Assume a solution to (A 17) of the form

$$u = \text{Re}\left(\sum_{n=1}^{\infty} A_n U_n(x)\, e^{it}\right), \tag{A 18}$$

$$p = \text{Re}\left(\sum_{n=1}^{\infty} B_n Q_n(x)\, e^{it}\right), \tag{A 19}$$

which upon substitution into (A 17) gives

$$\sum_{n=1}^{\infty} A_n(iU_n + \omega\hat{k} \times U_n) + \sum_{n=1}^{\infty} B_n\nabla Q_n = F, \tag{A 20}$$

which, noting from (A 4) that $\hat{k} \times U_n = -(i/\omega_n)U_n - (1/\omega_n)\nabla Q_n$, becomes

$$\sum_{n=1}^{\infty} i(1 - \omega/\omega_n)A_n U_n + \sum_{n=1}^{\infty}(B_n - \omega/\omega_n A_n)Q_n = F. \tag{A 21}$$

Now applying the inner product operation gives

$$A_n = \frac{\langle F, U_n \rangle/\langle U_n, U_n \rangle}{i(1 - \omega/\omega_n)}, \tag{A 22}$$

using (A 9) to eliminate the pressure term. Thus, if the U_n are a complete set and the A_n are calculated according to (A 22), from (A 21) the B_n are given by

$$B_n = \frac{\omega}{\omega_n}A_n. \tag{A 23}$$

Referring to §2, recall that the spatial structure U_n of a mode is given by (2.11):

$$U_n = i\frac{1}{1 - \omega_n^2}\left[\frac{dJ_m(2\lambda_n r)}{dr} + m\omega_n\frac{1}{r}J_m(2\lambda_n r)\right]\cos\left[k\pi(z/h + \tfrac{1}{2})\right]\, e^{im\phi}, \tag{A 24}$$

$$V_n = \frac{-1}{1 - \omega_n^2}\left[\omega_n\frac{dJ_m(2\lambda_n r)}{dr} + m\frac{1}{r}J_m(2\lambda_n r)\right]\cos\left[k\pi(z/h + \tfrac{1}{2})\right]\, e^{im\phi}, \tag{A 25}$$

$$W_n = -i\frac{k\pi}{h}J_m(2\lambda_n r)\sin\left[k\pi(z/h + \tfrac{1}{2})\right]\, e^{im\phi}. \tag{A 26}$$

The forcing term F from the right-hand side of the inhomogeneous equation for precessional forcing (2.2) is $-(\omega - 2)r\, e^{i\phi}\hat{k}$. To calculate $\langle F, U_n \rangle$, therefore, it is

necessary to evaluate the integral

$$\langle \boldsymbol{F}, \boldsymbol{U}_n \rangle = \int_{\mathscr{V}} -(\omega - 2)r \, e^{i\phi} W_n^{\dagger} \, d\mathscr{V} \tag{A 27}$$

$$= \int_{\mathscr{V}} (2 - \omega)r \, e^{i\phi} i(k\pi/h) J_m(2\lambda_n r) \sin\left[k\pi(z/h + \tfrac{1}{2})\right] \, e^{-im\phi} r \, dr \, d\phi \, dz \tag{A 28}$$

$$= i4\pi(2 - \omega) \int_0^{\frac{1}{2}} r^2 J_1(2\lambda_n r) \, dr, \quad m = 1 \text{ and } k \text{ odd}$$

$$= 0, \qquad\qquad\qquad m \neq 1 \text{ or } k \text{ even.} \tag{A 29}$$

Now calculate

$$\langle \boldsymbol{U}_n, \boldsymbol{U}_n \rangle = \int_{\mathscr{V}} \left(U_n U_n^{\dagger} + V_n V_n^{\dagger} + W_n W_n^{\dagger} \right) \, d\mathscr{V}, \tag{A 30}$$

where, using (A 26),

$$\int_{\mathscr{V}} U_n U_n^{\dagger} r \, dr \, d\phi \, dz = \frac{1}{(1 - \omega_n^2)^2} \int_{\mathscr{V}} \left[\frac{dJ_m(2\lambda_n r)}{dr} + m\omega_n \frac{1}{r} J_m(2\lambda_n r) \right]^2$$
$$\times \cos^2\left[k\pi(z/h + \tfrac{1}{2})\right] r \, dr \, d\phi \, dz \tag{A 31}$$

$$= \frac{\pi h}{(1 - \omega_n^2)^2} I_u, \tag{A 32}$$

where

$$I_u = \int_0^{\frac{1}{2}} \left[\frac{dJ_m(2\lambda_n r)}{dr} + m\omega_n \frac{1}{r} J_m(2\lambda_n r) \right]^2 r \, dr, \tag{A 33}$$

$$\int_{\mathscr{V}} V_n V_n^{\dagger} r \, dr \, d\phi \, dz = \frac{1}{(1 - \omega_n^2)^2} \int_{\mathscr{V}} \left[\omega_n \frac{dJ_m(2\lambda_n r)}{dr} + m\frac{1}{r} J_m(2\lambda_n r) \right]^2$$
$$\times \cos^2\left[k\pi(z/h + \tfrac{1}{2})\right] r \, dr \, d\phi \, dz \tag{A 34}$$

$$= \frac{\pi h}{(1 - \omega_n^2)^2} I_v, \tag{A 35}$$

where

$$I_v = \int_0^{\frac{1}{2}} \left[\omega_n \frac{dJ_m(2\lambda_n r)}{dr} + m\frac{1}{r} J_m(2\lambda_n r) \right]^2 r \, dr, \tag{A 36}$$

and

$$\int_{\mathscr{V}} W_n W_n^{\dagger} r \, dr \, d\phi \, dz = \left(\frac{k\pi}{h}\right)^2 \int_{\mathscr{V}} [J_m(2\lambda_n r)]^2 \sin^2\left[k\pi(z/h + \tfrac{1}{2})\right] r \, dr \, d\phi \, dz \tag{A 37}$$

$$= \pi h \left(\frac{k\pi}{h}\right)^2 \frac{1}{8} [J_{m+1}(\lambda_n)]^2, \tag{A 38}$$

by using the standard properties of Bessel functions. On adding (A 32), (A 35) and (A 38),

$$\langle \boldsymbol{U}_n, \boldsymbol{U}_n \rangle = \pi h \left[\frac{1}{(1 - \omega_n^2)^2} (I_u + I_v) + \left(\frac{k\pi}{h}\right)^2 \frac{1}{8} [J_{m+1}(\lambda_n)]^2 \right], \tag{A 39}$$

and so, from (A 21), (A 29) and (A 39), the amplitude of the nth mode is given by

$$A_n = \frac{4(2 - \omega) \int_0^{\frac{1}{2}} r^2 J_1(2\lambda_n r) \, dr}{(1 - \omega/\omega_n)h \left[1/(1 - \omega_n^2)^2 (I_u + I_v) + (k\pi/h)^2 \frac{1}{8}[J_2(\lambda_n)]^2 \right]}, \quad m = 1 \text{ and } k \text{ odd}$$

$$= 0, \quad m \neq 1 \text{ and } k \text{ even.} \tag{A 40}$$

From (A 26), the velocity $\mathbf{u} = \text{Re} \sum_{n=1}^{\infty}(A_n U_n \, e^{it})$ is given by

$$\mathbf{u} = \sum_{n=1}^{\infty} A_n \left\{ -\frac{1}{1 - \omega_n^2} \left[\frac{dJ_1(2\lambda_n r)}{dr} + \omega_n \frac{1}{r} J_1(2\lambda_n r) \right] \cos \left[k\pi(z/h + \tfrac{1}{2}) \right] \sin(\phi + t) \right.$$

$$\frac{-1}{1 - \omega_n^2} \left[\omega_n \frac{dJ_1(2\lambda_n r)}{dr} + \frac{1}{r} J_1(2\lambda_n r) \right] \cos \left[k\pi(z/h + \tfrac{1}{2}) \right] \cos(\phi + t)$$

$$\left. \frac{k\pi}{h} J_1(2\lambda_n r) \sin \left[k\pi(z/h + \tfrac{1}{2}) \right] \sin(\phi + t) \right\} \tag{A 41}$$

and the pressure by

$$p = \sum_{n=1}^{\infty} \frac{\omega}{\omega_n} A_n J_1(2\lambda_n r) \cos \left[k\pi(z/h + \tfrac{1}{2}) \right] \cos(\phi + t). \tag{A 42}$$

A.2. Calculating the fluid particle pathlines

Here we consider the determination of the fluid particle pathlines corresponding to a sum of linear inviscid modes. These modes comprise some of the forced modes, and the free mode with the largest amplitude.

Given the linear inviscid solution, the problem of calculating the fluid pathlines is twofold; firstly, the integrals giving A_n in (A 40) must be calculated, and secondly, we must solve the three nonlinearly coupled ordinary differential equations (A 26) for $r(t), \phi(t)$ and $z(t)$. Numerical Algorithms Group (NAG) routines were used throughout, coded in double-precision FORTRAN and run on the Cambridge IBM 3084.

The integrals in the term A_n were calculated with a third-order finite-difference scheme. The solution of (A 26) was done numerically with an adjustable-stepsize Runge–Kutta routine. The paths were calculated for dye particles released as passive tracers at a succession of points along a hypothetical wire.

The actual motion during the tilt-out is modelled by making the nutation angle θ a function of time for the 0.1 s taken by the tilting motion. As noted in §5, the mechanical origin of the tilting motion leads this displacement to be modelled as the first quarter-period of a sine function that reaches its peak at 0.1 s.

Fourteen forced modes are included in the calculation; they are tabulated in table 2. It was found that for the parameters of the experiments reported here, the (1,1,1) mode, which was being forced near resonance, so dominated the response that it accounted for 90–95% of the velocity field.

It was decided that one free mode, the (1,1,1) mode, should be included since its structure best represents the initial tilt disturbance applied to the system. The free mode's response was only estimated, rather than calculated by mode projection integrals as in §A.1, since the actual velocities during the impulsive tilt were unknown,

k	l	ω_{kl1}	λ_{kl1}	k	l	ω_{kl1}	λ_{kl1}
1	1	2.64298	2.88223	3	3	2.69398	8.84105
1	1	-4.05609	4.63098	5	1	1.08229	2.43832
1	2	5.27757	6.10482	5	2	1.37830	5.58728
1	2	-6.73255	7.84364	5	3	1.78975	8.74335
1	3	7.93762	9.27674	7	1	1.04224	2.42220
3	1	1.22370	2.49273	7	2	1.20585	5.55698
3	2	1.89134	5.67388	7	3	1.45410	8.70569

TABLE 2. Modes used in the forced response calculation

rendering further precision in this part of the calculation unproductive. Therefore, the free mode response was estimated by assuming that the 'impulsive' velocity initially imparted to the fluid during the tilt-out later gets represented by a freely oscillating (1,1,1) mode. The impulsive velocity (in tank coordinates) due to the tilt was estimated, together with the velocity due to the Coriolis force acting over this period, from the calibrations in Manasseh (1991). This estimate was made near the tank ends (where it is a maximum) and matched by a freely oscillating (1,1,1) mode with appropriate amplitude and phase to account for the estimated velocity at the ends.

At time $t = 0$ the particles are located on a hypothetical wire at $r = 0.25$, $\phi = 3\pi/2$ and parallel to the z-axis. The integrations were performed to a non-dimensional time of 5 revolutions. The timelines corresponding to the loci of the positions of a succession of particles were also calculated. A line has been plotted at $t = 0$ to mark the wire. Timelines have been plotted at $t = \pi$, and at each revolution thereafter, on the (r, z) projection shown in figure 3.

Further details on the calculation and cross-checks against other methods are in Manasseh (1991).

REFERENCES

ALDRIDGE, K. D. & STERGIOPOULOS, S. 1991 A technique for direct measurement of time–dependent complex eigenfrequencies of waves in fluids. *Phys. Fluids* A **3**, 316–327.

BAKER, J. D. 1966 A technique for the precise measurement of small fluid velocities. *J. Fluid Mech.* **26**, 573–575.

FULTZ, D. 1959 A note on overstability, and the elastoid-inertia oscillations of Kelvin, Solberg and Bjerknes. *J. Meteorol.* **16**, 199–208.

GLEDZER, E. B., DOLZHANSKII, F. V. & OBUKHOV, A. M. 1989 Instability of elliptical rotation and simple models of vortex fluid flows. *Abstracts, Euromech 245: The effect of background rotation on fluid motions, Dept. Applied Math. & Theor. Physics, Cambridge, UK, April 10–13, 1989.*

GLEDZER, E. B. & PONOMAREV, V. M. 1992 Instability of bounded flows with elliptical streamlines. *J. Fluid Mech.* **240**, 1–30.

GREENSPAN, H. P. 1968 *The Theory of Rotating Fluids.* Cambridge University Press.

GUNN, J. S. & ALDRIDGE, K. D. 1990 Inertial wave eigenfrequencies for a non-uniformly rotating fluid. *Phys. Fluids* A **2**, 2055–2060.

KELVIN, LORD 1880 Vibrations of a columnar vortex. *Phil. Mag.* **10**, 155–168.

KERSWELL, R. R. 1993 The instability of precessing flow. *Geophys. Astrophys. Fluid Dyn.* **72**, 107–144.

KUDLICK, M. D. 1966 On transient motions in a contained rotating fluid. PhD. thesis, Massachusetts Institute of Technology.

MALKUS, W. V. R. 1968 Precession of the Earth as the cause of geomagnetism. *Science* **160**, 259–264.

MALKUS, W. V. R. 1989 An experimental study of the global instabilities due to the tidal (elliptical) distortion of a rotating elastic cylinder. *Geophys. Astrophys. Fluid Dyn.* **48**, 123–134.

MALKUS, W. V. R. & WALEFFE, F. A. 1991 Transition from order to disorder in elliptical flow: a direct path to shear flow turbulence. In *Advances in Turbulence 3* (ed. A. V. Johansson & P. H. Alfredsson), pp. 197–203. Springer.

MANASSEH, R. 1991 Inertia Wave breakdown: experiments in a precessing cylinder. PhD thesis, University of Cambridge.

MANASSEH, R. 1992 Breakdown regimes of inertia waves in a precessing cylinder. *J. Fluid Mech.* **243**, 261–296.

MANASSEH, R. 1993 Visualization of the flows in precessing tanks with internal baffles. *Am. Inst. Aeronaut. Astronaut. J.* **31**, 312–318.

McEWAN, A. D. 1970 Inertial oscillations in a rotating fluid cylinder. *J. Fluid Mech.* **40**, 603–640.

McINTYRE, M. E. & NORTON, W. A. 1990 Dissipative wave-mean interactions and the transport of vorticity or potential vorticity. *J. Fluid Mech.* **212**, 403–435.

SCOTT, P. R. & TAN, D. G. H. 1993 Complex-frequency method for computing the dynamics of liquid in a spinning container. *J. Guidance, Control Dyn.* **16**, 190–196.

STERGIOPOULOS, S. & ALDRIDGE, K. D. 1982 Inertial waves in a fluid partially filling a cylindrical cavity during spin-up from rest. *Geophys. Astrophys. Fluid Dyn.* **21**, 89–112.

TAN, D. G. H. 1991 Dynamics of a rotating body containing a liquid-filled cavity. *Final Report* (Volume 2). Dept. Applied Math. & Theor. Physics, University of Cambridge.

THOMPSON, R. 1970 Diurnal tides and shear instabilities in a rotating cylinder. *J. Fluid Mech.* **40**, 737–751.

WALEFFE, F. 1990 On the three dimensional instability of strained vortices. *Phys. Fluids* A **2**, 76–80.

WOOD, W. W. 1966 An oscillatory disturbance of rigidly rotating fluid. *Proc. R. Soc. Lond.* A **293**, 181–212.